

A Strontium Quantum-Gas Microscope

Sandra Buob¹, Jonatan Höschele¹, Vasiliy Makhlov¹, Antonio Rubio-Abadal^{1,*} and Leticia Tarruell^{1,2,†}

¹ICFO—Institut de Ciències Fotoniques, The Barcelona Institute of Science and Technology,
08860 Castelldefels (Barcelona), Spain

²ICREA, Pg. Lluís Companys 23, 08010 Barcelona, Barcelona, Spain



(Received 22 December 2023; accepted 22 March 2024; published 18 April 2024)

The development of quantum-gas microscopes has brought novel ways of probing quantum degenerate many-body systems at the single-atom level. Until now, most of these setups have focused on alkali atoms. Expanding quantum-gas microscopy to alkaline-earth elements will provide new tools, such as SU(N)-symmetric fermionic isotopes or ultranarrow optical transitions, to the field of quantum simulation. Here we demonstrate the site-resolved imaging of a ^{84}Sr bosonic quantum gas in a Hubbard-regime optical lattice. The quantum gas is confined by a two-dimensional in-plane lattice and a light-sheet potential, which operate at the strontium clock-magic wavelength of 813.4 nm. We realize fluorescence imaging using the broad 461-nm transition, which provides high spatial resolution. Simultaneously, we perform attractive Sisyphus cooling with the narrow 689-nm intercombination line. We reconstruct the atomic occupation from the fluorescence images, obtaining imaging fidelities above 94%. Finally, we realize a ^{84}Sr superfluid in the Bose-Hubbard regime. We observe its interference pattern upon expansion, a probe of phase coherence, with single-atom resolution. Our strontium quantum-gas microscope provides a new platform to study dissipative Hubbard models, quantum optics in atomic arrays, and SU(N) fermions at the microscopic level.

DOI: 10.1103/PRXQuantum.5.020316

I. INTRODUCTION

The ability to control and detect individual particles has been a major driving force in the field of quantum science and technology. A prime example is given by quantum-gas microscopes [1], which are an extremely versatile tool for the analog quantum simulation of Hubbard models. These are devices that provide access to the microscopic properties of quantum gases in optical lattices through site-resolved detection of single atoms. Quantum-gas microscopy, demonstrated for both bosons [2,3] and fermions [4–7], has provided a microscopic point of view on fundamental problems of quantum magnetism [8–11], transport properties in many-body systems [12–14], and quantum thermalization [15–17], among other examples. Most microscope setups to date have been realized with alkali atoms, which have only one

valence electron. Extending quantum-gas microscopy to other atomic species opens exciting opportunities for quantum simulation. So far, examples of beyond-alkali microscopes include microscopes based on bosonic ytterbium [18–20] and highly magnetic erbium [21].

Atomic species with two valence electrons, such as alkaline-earth and alkaline-earth-like atoms, are of special interest for quantum simulation [22]. Their distinct electronic structure, with singlet and triplet states, gives rise to narrow and ultranarrow optical transitions, which can be used as a precise probe, and to long-lived metastable states in which quantum information can be stored [23]. Furthermore, fermionic isotopes with a nuclear spin display interparticle interactions that are independent of their magnetic state, hence allowing the study of SU(N)-symmetric systems [24]. Many of these properties have been exploited in recent optical-lattice studies that relied on global observables. Some examples include spin-orbit coupling using the metastable clock state [25,26], dissipative Bose-Hubbard models [27,28], and SU(N) fermions [29–32].

Atomic strontium has become a popular choice for the aforementioned research fields. It has one fermionic and several bosonic stable isotopes, which have been successfully brought to quantum degeneracy [33–36]. The

*Corresponding authors: antonio.rubio@icfo.eu
†leticia.tarruell@icfo.eu

Published by the American Physical Society under the terms of the [Creative Commons Attribution 4.0 International license](#). Further distribution of this work must maintain attribution to the author(s) and the published article's title, journal citation, and DOI.

fermionic isotope ^{87}Sr features a large nuclear spin, leading to an $\text{SU}(N = 10)$ symmetry. Furthermore, the ultra-narrow transition at 698 nm finds application in optical atomic clocks [37], which rely on state-insensitive traps at magic wavelengths [38]. This set of favorable properties for quantum simulation makes the development of a strontium quantum-gas microscope highly desirable.

Single-atom imaging of strontium atoms was recently achieved in optical tweezers [39,40], by use of the short wavelength of its blue, 461-nm transition and the cooling properties of its red, 689-nm intercombination line. Additionally, hybrid lattice-tweezer platforms have been developed, which have demonstrated single-atom imaging of strontium in optical lattices [41,42] and realized programmable quantum walks [43,44]. However, these studies of hybrid systems have so far focused on the ^{88}Sr isotope, which, due to its negligible scattering length, precludes attaining the interacting Hubbard regime or reaching quantum degeneracy through evaporative cooling.

In this work, we demonstrate the realization of a strontium quantum-gas microscope. We achieve this by combining the preparation of a quantum degenerate cloud of ^{84}Sr , an interacting bosonic isotope, with the imaging techniques pioneered by the optical-tweezer community. An evaporatively cooled ^{84}Sr cloud is confined in a 2D geometry by a highly anisotropic light-sheet optical trap and is loaded into an in-plane square optical lattice, all operating at 813.4 nm. This wavelength is magic for the strontium clock transition [38]. For the imaging stage, the confinement is brought to its maximum experimentally available depth and then fluorescence photons, scattered at the broad-linewidth blue transition, are collected with a high-numerical-aperture objective. The atoms are simultaneously cooled within their lattice sites by use of the narrow-linewidth red transition. We realize this in a configuration with a tighter confinement for the 3P_1 excited state than for the 1S_0 ground state. This difference leads to the so-called attractive Sisyphus cooling [47], which we demonstrate here in an optical lattice. The high efficiency of this cooling approach highlights that quantum-gas microscopy can be realized with moderate laser powers and in a setup with reduced experimental complexity. Finally, by preparing a quantum gas in a shallow optical lattice, we realize a superfluid in the Bose-Hubbard regime, and detect the interference pattern arising during its expansion due to phase coherence.

This article is organized as follows: In Sec. II we describe the main elements of the experimental setup, and the techniques required for single-atom imaging. In Sec. III we present a reconstruction of raw fluorescence images and benchmark the site-resolved imaging fidelity of the experiment. In Sec. IV we discuss the spatial dependence of Sisyphus cooling and how the overall confinement in the system can be characterized from it. In Sec. V we discuss the loading of a degenerate gas into the optical lattice and

show its interference pattern after expansion, which showcases the phase coherence of a lattice superfluid. Finally, we conclude by summarizing the main results and possible future directions in Sec. VI.

II. EXPERIMENTAL SETUP

The experiment is performed in a glass cell with a high-resolution objective placed immediately below, which constitute the central pieces of the experimental setup; see Figs. 1(a)–1(c). Inside the glass cell, we trap and cool ^{84}Sr atoms to quantum degeneracy before loading them into an optical lattice and imaging them with single-site resolution.

A. Preparation of a quantum gas

For cooling and trapping, we apply the common two-stage magneto-optical trap (MOT) scheme of strontium experiments (see Appendix A and our previous work [48]). This results in a cloud of 5×10^5 atoms with temperatures of a few microkelvins. This cold cloud is subsequently loaded into a crossed optical dipole trap, consisting of two 1064-nm laser beams each at a power of 3 W. This results in a potential depth of 20 μK where we initially trap 10^5 atoms. While holding them in the crossed trap, we ramp up a light-sheet potential, which is a tightly focused elliptical beam at the clock-magic wavelength of strontium, 813.4 nm [see Fig. 1(a)]. The light-sheet-beam waists of $3.5 \mu\text{m} \times 60 \mu\text{m}$ result in a trap depth of 50 μK at a power of 270 mW. Taking advantage of the favorable scattering length of ^{84}Sr , $a_s = 123a_0$ [33,34], we perform evaporative cooling in this combined potential for 8 s. To this end, we exponentially decrease the power of the crossed trap beams to zero and the light-sheet potential to a finite depth. After this stage, we reach a quantum degenerate gas of typically around 300 atoms and no discernible thermal fraction.

B. Square optical-lattice potential

We generate the lattice potential with a $\lambda = 813.4$ nm vertically polarized beam, which travels in a bow-tie configuration twice through the glass cell before being retroreflected; see Fig. 1(a). This configuration results in the interference of four beams, which all share the same polarization $\vec{\epsilon}_{813}$. The interference leads to a square lattice with spacing $\lambda/\sqrt{2} \approx 575$ nm [49], as depicted in Fig. 1(b), which we use both as a physics lattice and as an imaging lattice. Additionally, it makes phase stabilization redundant and allows us to recycle the power of the beam. This is highly beneficial for high-depth applications during imaging in quantum-gas microscopes [50–52]. We achieve a full lattice depth of up to 140 μK with a total lattice power of 3 W. This corresponds to $800 E_r$, where $E_r = h^2/2m\lambda^2 \approx h \times 3.6 \text{ kHz}$ is the recoil energy of the

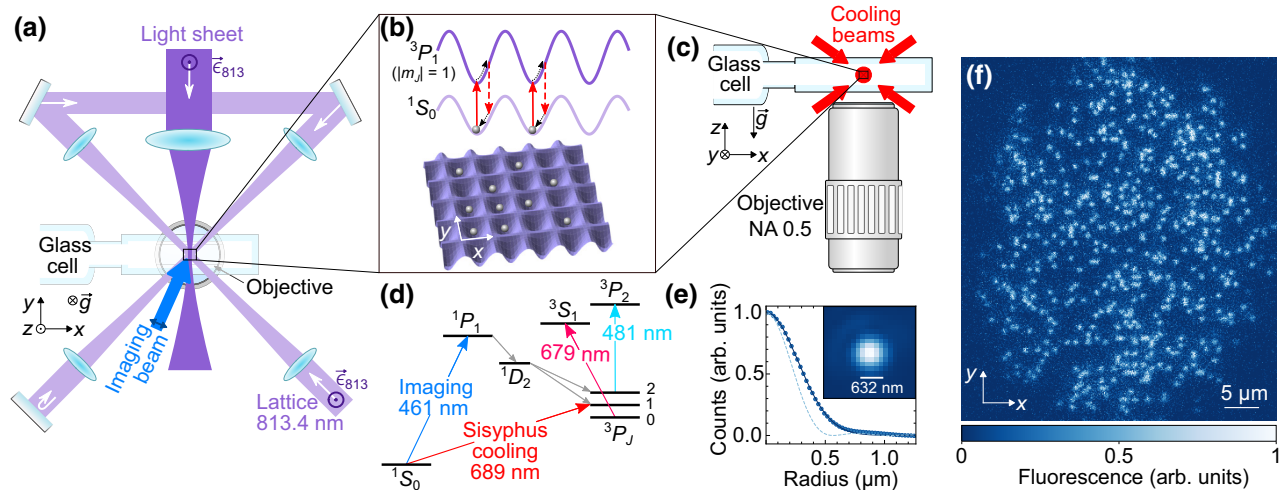


FIG. 1. Strontium quantum-gas microscope. (a) Top view of the experimental setup, showing the lattice beam passing four times through the quartz glass cell. The light-sheet beam is tightly focused (waist in the z direction approximately $3.5\ \mu\text{m}$) and provides the vertical confinement into the plane. The lattice and light-sheet beams are vertically polarized ($\vec{\epsilon}_{813}$) and operate at a wavelength of $813.4\ \text{nm}$. The objective, placed below the glass cell, captures the fluorescence signal of the atoms generated by a blue imaging beam at $461\ \text{nm}$ that is horizontally polarized. (b) Two-dimensional potential created by the fourfold interference of the lattice beams (bottom). The tighter confinement in the 3P_1 excited state compared with the 1S_0 ground state (top) allows attractive Sisyphus cooling on the red intercombination transition at $689\ \text{nm}$. (c) Side view of the experimental setup, depicting the six red cooling beams and the objective placed below the glass cell. (d) Energy-level diagram of strontium, with the broad-linewidth imaging transition and the narrow-linewidth cooling transition. Shown are also the repumping transitions ($481\ \text{nm}$ [45] and $679\ \text{nm}$ [46]) used to recover atoms that leaked into the long-lived states 3P_0 and 3P_2 . (e) Azimuthal average of the PSF (blue circles), with a Gaussian fit (solid line) and the ideal Airy disk (dashed line). The inset shows the PSF obtained by averaging the signal of 1187 isolated atoms. (f) Raw fluorescence image of a dilute thermal cloud showing around 500 individual ^{84}Sr atoms. NA, numerical aperture.

lattice beam photons. Here h is Planck's constant and m is the mass of ^{84}Sr .

C. In-lattice Sisyphus cooling

An efficient cooling mechanism is required to preserve the atoms in their individual lattice sites during imaging. For atomic strontium, the narrow linewidth of the red transition can be exploited for resolved sideband cooling, which requires equal trapping frequencies for ground and excited states ($\omega_g = \omega_e$) [38,53]. Imaging of individual strontium atoms has been shown with this technique by tuning to a magic configuration in both optical tweezers and optical lattices [39–41]. A different approach, available in the case of nonzero differential trapping, is Sisyphus cooling [54,55]. Depending on the sign of the differential trapping, this method can be realized in either the repulsive regime ($\omega_g > \omega_e$) or the attractive regime ($\omega_g < \omega_e$). Single-atom imaging in the repulsive Sisyphus regime has been demonstrated in optical tweezers [40] and lattices [42], while in the attractive regime it has been shown only in optical tweezers [40,47].

In our experiment, we perform attractive Sisyphus cooling in an optical lattice. As depicted in Fig. 1(b), the excited states with $|m_J| = 1$ experience a deeper trapping potential than the ground state. This is the case when a

magnetic bias field is parallel to the lattice and light-sheet polarization, i.e., $\vec{B} \parallel \vec{\epsilon}_{813}$. As atoms are excited from the bottom of the trap via the 689-nm transition, they will experience an average reduction of energy through spontaneous emission, due to the steeper potential of the excited state. While Sisyphus cooling can be realized with a single laser beam [47], here we use the same set of laser beams as for the red MOT stage, see Fig. 1(c), reducing the complexity of the experimental setup. The total intensity of the beams during imaging is on the order of $1000 I_{s,\text{red}}$, where $I_{s,\text{red}}$ is the saturation intensity of the red transition. The frequency is set to the light-shifted resonance, which in the center of the cloud is up to 1.3 MHz red detuned from its free-space value (see Appendix C). Because of light-assisted collisions, the cooling process also induces parity projection to the occupation in each lattice site [40].

During the imaging stage, both the lattice and the light sheet are brought to their greatest depth, with on-site trapping frequencies $\omega_{x,\text{site}} \approx 2\pi \times 150\ \text{kHz}$, $\omega_{y,\text{site}} \approx 2\pi \times 140\ \text{kHz}$, and $\omega_{z,\text{site}} \approx 2\pi \times 6.5\ \text{kHz}$. Efficient intrapool cooling typically requires Lamb-Dicke parameters $\eta_i = \sqrt{h\pi/m\omega_i\lambda_c^2} < 1$ for its three axes $i = x, y, z$, where λ_c is the wavelength of the cooling transition. In our case, for $\lambda_c = 689\ \text{nm}$, we obtain a small in-plane parameter $\eta_x \approx \eta_y \approx 0.2$ and an axial parameter $\eta_z \approx 0.9$. We observe efficient cooling even with such a weak axial

confinement, which is consistent with a recent result obtained with attractive Sisyphus cooling in shallow optical tweezers [56].

D. High-resolution fluorescence imaging

The fluorescence imaging of the atoms is realized by scattering photons on the broad-linewidth 461-nm transition, through a near-resonant beam shone into the atomic cloud. The photons are collected by a high-resolution infinity-corrected objective (G Plan Apo 50X, Mitutoyo) with a numerical aperture of 0.5. The objective is placed at its working distance of 15.08 mm from the atoms, outside a quartz glass cell of 3.5-mm thickness [see Fig. 1(c)]. The imaging system consists additionally of an achromatic doublet (ACT508-500-A, Thorlabs), which leads to a measured magnification of 126.7(3). The fluorescence photons are detected by an electron multiplying CCD camera (Andor iXon Ultra 897) with 85 % quantum efficiency at 461 nm and a pixel size of 16 μm .

To induce fluorescence, we shine a linearly polarized blue laser with $I \sim 10^{-3} I_{s,\text{blue}}$, detuned from resonance by $\delta \approx -2 \Gamma_{\text{blue}}$. Here $I_{s,\text{blue}}$ and Γ_{blue} are, respectively, the saturation intensity and the linewidth of the blue transition. The linear polarization is chosen to be in plane, which ensures optimal collection efficiency of the radiation pattern [40]. From the intensity and detuning, we estimate a scattering rate of approximately 3 kHz, which takes into account the simultaneous saturation of the red-cooling transition. The imaging system has an estimated collection efficiency of 6.7 % (71 % transmission of the path, and an objective collection efficiency of 9.4 %). In our pictures, we typically detect around 300 photons per atom during a 3-s exposure. In Fig. 1(f), we show a fluorescence image of a thermal cloud with around 500 atoms. In addition to the blue beam, we simultaneously shine two repumping beams to recover atoms that leaked into the long-lived 3P_2 and 3P_0 states; see Fig. 1(d).

On the basis of the numerical aperture of the objective, we estimate a Rayleigh resolution of 562 nm, which corresponds to a full width at half maximum of 470 nm. Such a resolution is below the 575-nm lattice spacing of the four-fold optical lattice, and can hence resolve the atoms in the individual sites. To characterize our imaging system, we measure its point spread function (PSF); see Fig. 1(e). For this purpose, we capture the fluorescence signal of isolated atoms in sparsely filled lattices and we overlap and average their signal. From the resulting PSF, we find a full width at half maximum of 632(3) nm. This value is greater than the ideal expectation, but it is sufficiently small to resolve individual lattice sites in the system.

III. IMAGE RECONSTRUCTION AND PINNING FIDELITY

To access the microscopic properties of the cloud, one has to reconstruct the atomic occupation from the

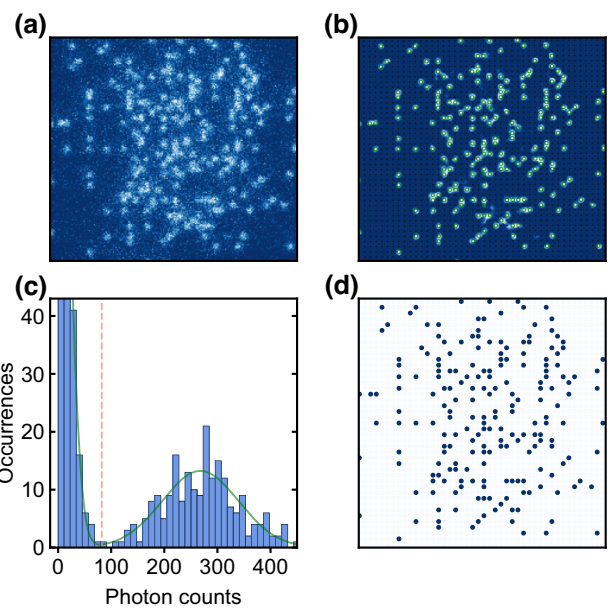


FIG. 2. Reconstruction of the atomic occupation from a fluorescence image. (a) Raw experimental image of a thermal cloud loaded in the lattice. (b) Deconvolution of the image in (a) with the PSF to obtain a cleaner signal. The black circles mark the positions of the reconstructed lattice grid, while the green circles indicate the lattice sites detected as occupied. (c) Histogram of the counts at each lattice site for the deconvolved picture in (b). The plot indicates the distinguishability between the zero-atom case (left peak) and the one-atom case (right peak). To choose the threshold value in counts, we fit a double Gaussian function to the histogram. From the fit we estimate that more than 99.9% of the one-atom distribution lies above the threshold in this image. (d) Binary occupation obtained from the reconstruction of the picture.

fluorescence images and hence obtain the site-resolved distribution; see Fig. 2. As a first step, the captured images are deconvolved with the measured PSF of the system by realizing 15 iterations of the Richardson-Lucy algorithm [57,58]. The resulting image, shown in Fig. 2(b), is Fourier transformed to extract the lattice vectors and their phase, which enable a full reconstruction of the lattice grid. From the lattice reconstruction, we find an anisotropy in the lattice spacing, with $a_x = 608(1)$ nm and $a_y = 547(1)$ nm. It can be explained by a deviation of the interfering beams from the ideal 90° angles; see Appendix A. With the lattice reconstructed, we bin the photon counts at each lattice site to obtain the histogram in Fig. 2(c). By setting a threshold for the number of binned photon counts, we are able to discriminate occupied lattice sites from empty ones, which we display in Fig. 2(d). The separation between the zero-photon peak and the right peak, which is centered at around 300 photon counts, indicates a reliable detection of single-occupied sites.

To benchmark the imaging fidelity of our system, we measure a set of pairs of consecutive images of the same

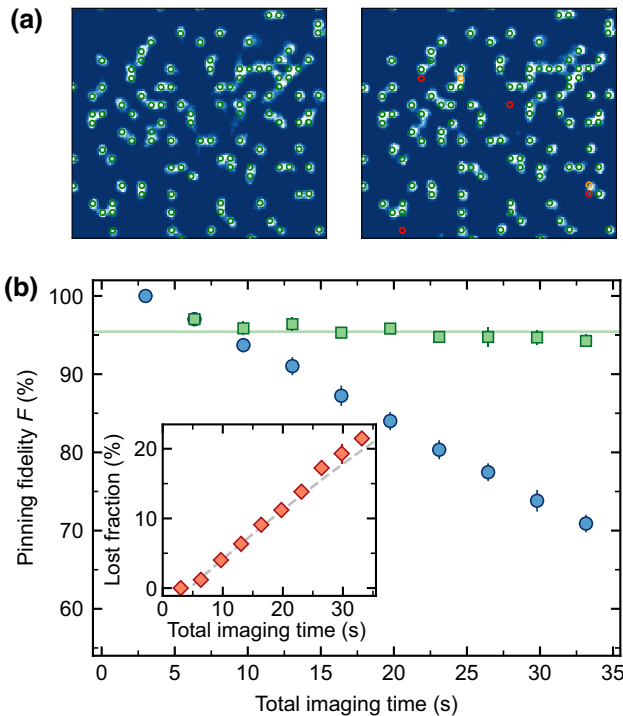


FIG. 3. Fidelity of the site-resolved single-atom detection. (a) Two consecutive images ($15.5 \times 15.5 \mu\text{m}^2$ region) of the same cloud after being deconvolved. In the first picture, the one on the left, we mark sites where an atom has been detected with green circles. In the second picture, the one on the right, lost atoms are indicated with red circles, atoms that hopped are indicated in orange, and those that remained in the same position are indicated in green. The single-shot pinning fidelity F is 96.5%. (b) Pinning fidelity F as a function of imaging time. We take ten images of the same cloud within 35 s and compare the reconstructed occupation with either the occupation corresponding to the initial shot (blue circles) or the occupation corresponding to the previous shot (green squares). The solid green line marks the average of all green-square fidelity data, which is around 95%. The inset shows the accumulated losses for each consecutive measurement (red diamonds) compared with those caused by background-gas losses (dashed gray line). Error bars indicate one standard error of the mean.

atomic cloud, applying the reconstruction algorithm to both images. This allows us to identify loss and hopping events from one shot to the next one, and to estimate the pinning fidelity, i.e., the fraction of atoms that remain in their original sites in the second image. In Fig. 3(a) we show the deconvolutions of two exemplary consecutive images. The green circles in the picture on the left indicate the sites where an atom has been detected. In the picture on the right, green circles indicate atoms identified in both pictures, red circles indicate atoms that have left their original site, and orange circles indicate newly identified atoms, i.e., hopping events. From averaging over 47 such pairs of images (10% average density over a $25 \times$

$25 \mu\text{m}^2$ region), we extract a pinning fidelity of 94.1(2)% , a hopping fraction of 1.54(14)%, and a loss fraction of 4.3(3)%.

To further characterize the cooling efficiency and pinning fidelity of the system, we take a set of ten consecutive images for the same realization, similarly as in Ref. [52]. In Fig. 3(b), we show the pinning fidelity with respect to the first picture of the set (blue circles), which after 35 s of imaging has decreased to approximately 70%. We also extract the relative fidelity between consecutive images (green squares), which is shown to stay around 95% over the whole imaging time. We use this measurement to extract the losses as a function of imaging time, as shown in the inset (red diamonds). These losses are almost entirely explained by those associated with background-gas collisions, measured in the lattice without blue imaging light (dashed gray line) and characterized by an exponential decay constant $\tau_{\text{loss}} = 130(5)$ s. This is evidence that, for the imaging parameters chosen, losses associated with the imaging process are essentially negligible.

IV. SPATIAL DEPENDENCE OF SISYPHUS COOLING

Sisyphus cooling displays an intrinsic dependence of the cooling resonance on the trap intensities, due to the finite differential ac Stark shift between ground and excited states. This implies that the cooling performance is sensitive to the overall shape of the system confinement, and hence can be used as a tool to characterize it. In the configuration of our setup, with $\vec{B} \parallel \vec{\epsilon}_{813}$, the ground state and excited state polarizabilities are given by $\alpha_g = 286.0$ a.u. and $\alpha_e = 353.9$ a.u. [59], which corresponds to $\omega_g/\omega_e = \sqrt{\alpha_g/\alpha_e} \approx 0.9$. To characterize the spatial inhomogeneity of the system, here we study the cloud sizes of fluorescence images for different frequencies of the cooling laser.

In Fig. 4, we show four fluorescence images of large thermal clouds for increasing frequencies of the cooling laser. The first image displays a small elliptical cloud, explained by efficient cooling in the center and a complete atom loss in its outer edges. As the cooling frequency is increased, the red light gets closer to resonance with the atoms in the boundary. These atoms in turn experience a smaller light shift, and the fluorescent cloud size increases. Eventually, for even higher frequencies, the center of the cloud is no longer efficiently cooled, and losses lead to a density reduction in that region. In practice, we select a red-laser frequency that ensures efficient cooling, as indicated by the local pinning fidelities F , over the entire size of the prepared system. This is obtained at the expense of a reduced field of view in the images.

The spectral dependence of the cloud size can be used to spatially characterize the overall potential experienced by

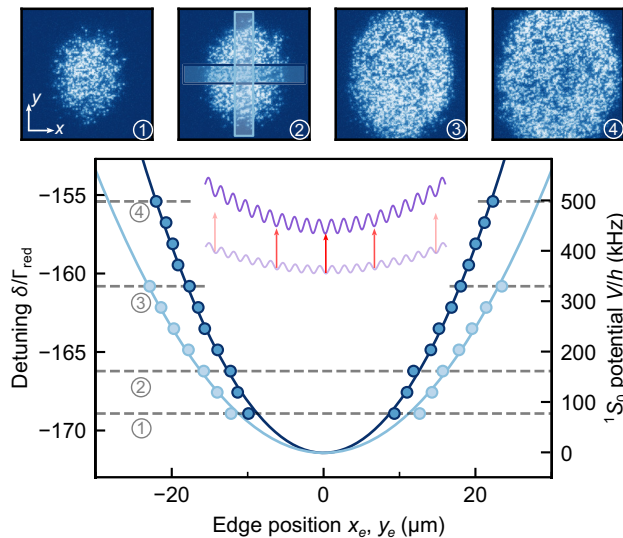


FIG. 4. Spatial inhomogeneity of Sisyphus cooling. Top: Four individual fluorescence images of atomic clouds at different red-cooling detunings. Frequencies closer to the free-space resonance lead to larger cloud sizes. Bottom: Red-cooling frequency corresponding to the position of the cloud edge. The edge positions of the cloud along the x and y axes are extracted by fitting an error function to the fluorescence signal within a sliced region (see the rectangular boxes in the second fluorescence image) integrated along the perpendicular direction. The shape allows us to extract the trapping frequency directly from the spectral dependence of the cloud size. The right axis indicates the potential V experienced by the ground state 1S_0 , computed from the differential polarizability. The inset in the lower plot illustrates the overall differential trapping, and how it shifts the red transition out of resonance. Horizontal dashed lines indicate the frequencies corresponding to the pictures at the top. The error bars are smaller than the marker size.

the atoms. To do so, we extract for each picture the positions of the two edges of the cloud along the x and y directions, which constitute equipotential points in the cloud. We realize this by selecting a region of interest for each direction (rectangular blue boxes in Fig. 4), integrating the fluorescence along the perpendicular direction, and fitting error functions to the resulting one-dimensional data. The fit parameters provide us with the edge values x_e and y_e for each cooling frequency. We present the results in Fig. 4, in which we plot the set cooling detunings as a function of the extracted edge positions. There, we identify the symmetric distribution of the frequencies around the center of the cloud, consistent with the light shift of a harmonic potential. Additionally, we infer the spatial potential experienced by the ground state 1S_0 , represented on the right axis, by using the known polarizabilities of the states involved. By performing a combined fit of the harmonic potentials for both directions, which share the same potential offset, we can extract the trapping frequencies of the overall potential, $\omega_{x,\text{image}} = 2\pi \times 497(2)$ Hz and $\omega_{y,\text{image}} = 2\pi \times$

387(2) Hz. The measured anisotropy in the trap frequencies, as indicated by the elliptical shape of the fluorescent clouds, originates from the elliptical confinement of the light sheet in the plane, which we measured independently via dipole oscillations to be $\omega_{x,\text{sheet}} = 2\pi \times 420(10)$ Hz and $\omega_{y,\text{sheet}} = 2\pi \times 252(5)$ Hz. The overall confinement, as characterized in Fig. 4, is compatible with the combination of the potentials from the light sheet and the optical-lattice envelope.

V. BOSE-HUBBARD SUPERFLUID

Finally, we use our quantum-gas microscope to perform single-site imaging of a ${}^{84}\text{Sr}$ superfluid in the Hubbard regime. While the images discussed in the previous sections were obtained by loading a thermal cloud into the lattice, here we perform evaporative cooling for $t_{\text{evap}} = 8$ s and load the resulting Bose-Einstein condensate adiabatically into a shallow optical lattice. For lattice depths $V_0 \gtrsim 2 E_r$, we expect the tight-binding approximation to hold and the system to be described by the 2D Bose-Hubbard model with tunneling amplitude J and interaction strength U . For $J/U > 0.06$ [60] the cloud should be in a superfluid phase with phase coherence across the entire system. This is the case in our setup for depths V_0 of $2 E_r$ to $5 E_r$ due to the relatively weak vertical confinement of approximately 1.1(1) kHz used in the experiments reported in this section. As before, E_r is defined in terms of the single-photon recoil and not in terms of the lattice spacing; see Appendix B.

Figure 5(a) shows an *in situ* image of an evaporatively cooled cloud loaded into a lattice of depth $V_0 = 2.3(1) E_r$, for which we expect a superfluid state. For a lattice potential with isotropic spacing and depth, this corresponds to tunneling amplitude $J/h = 188(8)$ Hz and interaction strength $U/h = 121(3)$ Hz. In our system, the lattice-spacing anisotropy and the relative attenuation of

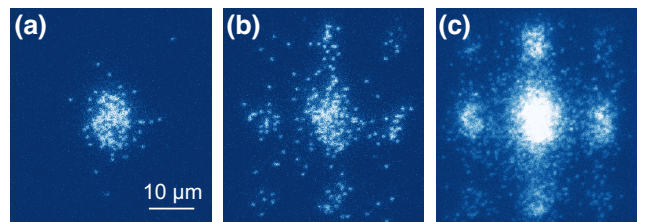


FIG. 5. Detection of a Bose-Hubbard superfluid. (a) *In situ* image of a quantum gas loaded into the optical lattice at a depth of $V_0 = 2.3(1) E_r$. (b) Image taken after an in-trap 2D expansion, during which the lattice is abruptly switched off for $t_{\text{exp}} = 2$ ms while the atoms are held in place by means of the harmonic trap produced by the light-sheet beam. An average over ten such pictures is displayed in (c), where higher-order interference peaks are visible at the corners of the image. The color scale in (c) has been adjusted to better discern the pattern.

the lattice beams leads to an asymmetry in the tunneling amplitudes. We estimate $J_x/J_y \approx 0.7$, see Appendix B, for which the system remains in the superfluid Hubbard regime.

An atomic superfluid in an optical lattice is commonly demonstrated by the observation of an interference pattern after a free-space time of flight [61]. Here we perform instead an in-plane expansion of the cloud within a shallow light-sheet potential after abruptly switching off the lattice potential. After the expansion, a sudden ramp-up of the lattice pins the atoms at their position, followed by site-resolved fluorescence imaging. In Fig. 5(b), we show a fluorescence image taken after an expansion for $t_{\text{exp}} = 2$ ms, where we observe the interference pattern. An important advantage of this method is that it enables the detection of phase coherence in the system even with low atom numbers (typically a few hundred), as previously shown in other quantum-gas experiments [2,62]. In our system, the anisotropy in the light-sheet confinement, with frequencies $\omega_{x,\text{exp}} = 2\pi \times 62.0(7)$ Hz and $\omega_{y,\text{exp}} = 2\pi \times 38.8(8)$ Hz, leads to an asymmetric expansion in the two in-plane directions. The expansion time chosen, $t_{\text{exp}} = 2$ ms, corresponds to $T_x/8 = (2\pi/\omega_x)/8$. Mapping of the momentum distribution at $t_{\text{exp}} = 0$ into the density distribution requires in-trap expansion of $T/4$ [63]. Here, we deliberately choose a smaller expansion time value of $T_x/8$ to avoid the emergence of high-density peaks, associated with the sharp momentum distribution of the superfluid in the lattice, and hence reduce the atom losses due to parity projection. This imaging technique allows us to capture higher-order interference peaks, which can be observed in the corners of the averaged image in Fig. 5(c). Having demonstrated the realization of a strontium quantum gas in the Bose-Hubbard regime, a natural next step will be the preparation of a unit-filled Mott insulator. This will be achieved by increasing the vertical confinement with a vertical optical lattice, which will soon allow us to reach the strongly interacting regime.

VI. CONCLUSION AND OUTLOOK

In this work we have demonstrated site-resolved imaging of ^{84}Sr atoms in a square optical lattice. The imaging was assisted by the realization of attractive Sisyphus cooling in an optical lattice. This technique has allowed us to realize a quantum-gas microscope with modest total laser powers (approximately 3 W at 813.4 nm). In addition, we have probed the phase coherence in the system to demonstrate the realization of a strontium superfluid in the Hubbard regime. Since the entire atomic confinement is realized with use of the clock-magic wavelength of 813.4 nm, our setup is ready for spectroscopy measurements using the optical clock transition, enabling high-precision measurements of single-body and many-body features [64–67].

At its current stage, the experimental setup is already capable of realizing microscopic studies of dissipation in the Bose-Hubbard model [27,28]. Another exciting research direction is that of collective light-matter phenomena in subwavelength atomic arrays [68,69], which we could realize by preparing a unit-filled Mott insulator. This is particularly exciting for strontium, since it exhibits micron-wavelength transitions that can be used to induce long-range dipolar interactions [70]. Finally, we stress that, while the results in this work are restricted to one bosonic isotope, our setup is capable of working with all stable isotopes of strontium [48], and generalization of quantum-gas microscopy to the fermionic isotope ^{87}Sr should be straightforward. This will open the door to microscopic studies of $SU(N)$ fermions, providing access to strongly interacting synthetic quantum Hall systems [71] and exotic forms of quantum magnetism [32,72,73].

ACKNOWLEDGMENTS

We acknowledge discussions with S. Blatt, A. Kaufman, V. Klüsener, A. Park, P. Schauß, A. Young, J. Zeiher, and the other members of the ICFO Quantum Gases Experimental group. We thank M. Miranda for the band-structure calculations and S. Hirthe for contributions to the reconstruction algorithm and for a careful reading of the manuscript. We acknowledge funding from the European Union [HORIZON-CL4-2022-QUANTUM-02-SGA through PASQuanS2.1 (Grant Agreement No. 101113690); DAALI (Grant Agreement No. 899275); ERC SuperComp (Grant Agreement No. 101003295)], Ministry of Science and Innovation of Spain, and State Research Agency MCIN/AEI/10.13039/501100011 (LIGAS project PID2020-112687GB-C21, DYNAMITE QuantERA project PCI2022-132919 with funding from European Union NextGenerationEU, Equipamiento Científico Técnico EQC2018-005001-P, EQC2019-005699-P, and EQC2019-005706-P, Severo Ochoa CEX2019-000910-S, and PRTR-C17.I1 with funding from European Union NextGenerationEU and Generalitat de Catalunya), Fundació Cellex, Fundació Mir-Puig, and Generalitat de Catalunya (“Quàntica – Vall de la Mediterrània de les Ciències i les Tecnologies Quàntiques” Government Agreement GOV/51/2022, promoted by Secretary of Digital Policies of the Government of Catalonia, AGAUR SGR 2021-SGR-01448 and CERCA program). S.B. acknowledges support from MCIN/AEI/10.13039/501100011033 and ESF (Grant No. PRE2020-094414). J.H. acknowledges support from the European Union (Marie Skłodowska-Curie Actions, Grant No. 713729), V.M. acknowledges support from the Beatriz de Pinós Program and the Ministry of Research and Universities of the Government of Catalonia (Grant No. 2019-BP-00228), and A.R. acknowledges support from the

MCIN/AEI/10.13039/501100011033 (Juan de la Cierva Formación Grant No. FJC2020-043086-I).

APPENDIX A: DETAILS ON THE EXPERIMENTAL SETUP

To prepare a cold cloud, before evaporative cooling, we capture atoms coming from an atomic source in the quartz glass cell (external dimensions of $67 \times 20 \times 17$ mm 3 with a glass thickness of 3.5 mm) by means of a three-dimensional MOT operated on the blue, 461-nm transition (1S_0 to 1P_1) with linewidth $\Gamma/2\pi = 30.5$ MHz. We continuously drive the MOT with two repumper lasers at 481 nm [45] and 679 nm [46] to restore atoms leaking into the metastable states 3P_0 and 3P_2 . The same repumper lasers are used during fluorescence imaging; see Fig. 1(d). Additionally, we shield the atoms partially from losses of the blue MOT transition by resonantly driving the red, 689-nm transition, as described in our previous work [48]. In a second laser-cooling stage, we bring the atoms in a narrow-line red MOT to a temperature of a few microkelvins, exploiting the 7.4-kHz-wide intercombination line at 689 nm from 1S_0 to 3P_1 [74]. To maximize the transfer efficiency, we start the red MOT with frequency-broadened laser beams to address many velocity classes of the atoms [75,76]. We then proceed by narrowing it to a single-frequency red MOT, resulting in around 5×10^5 atoms at temperatures of a few microkelvins. Then, we load them into a 20-μK-deep optical dipole trap at 1064 nm, generated by a Nd:YAG laser (Mephisto MOPA 25 W). This far-detuned crossed optical dipole trap consists of two beams with a waist of approximately 100 μm at an initial power of 3 W, propagating in plane and orthogonal to each other. We use it to load the atoms into the light-sheet trap as described in the main text. For the light sheet and the lattice, which form the imaging potential, we use a Ti:sapphire laser (Matisse CS pumped by a Millenia eV 25-W laser) at 813.4 nm. Since both trap beams have the same vertical polarization, we avoid their interference by shifting their frequencies by a few megahertz with respect to each other.

APPENDIX B: OPTICAL LATTICE

The bow-tie configuration of the optical-lattice beams results in a fourfold interference, as depicted in Fig. 1(a). Thus, the lattice potential can be written as

$$V_{\text{lat}}(x, y) = -\frac{V_0}{4} \{\cos^2(kx) + \cos^2(ky) + 2 \cos(kx) \cos(ky)\}, \quad (\text{B1})$$

where $k = 2\pi/\lambda$ describes the wave vector, with $\lambda = 813.4$ nm. V_0 is the full lattice depth, which displays a four-fold increase with respect to the single-retroreflected-beam case. Moreover, the lattice spacing is $\lambda/\sqrt{2} \approx 575$ nm and

not $\lambda/2 \approx 407$ nm. In this work, we express V_0 in terms of the recoil energy $E_r = h^2/2m\lambda^2 \approx h \times 3.6$ kHz of the lattice photons and not of the characteristic energy scale fixed by the lattice spacing $h^2/8ma^2 \approx h \times 1.8$ kHz. This is a convenient choice when one is considering alternative lattice geometries [49,77,78], which we plan to use in future experiments. Additionally, this definition is useful in the presence of small variations of the lattice spacing along the x and y directions, as those observed in our experiment ($a_x = 608(1)$ nm and $a_y = 547(1)$ nm). This spacing anisotropy stems from a small deviation of the lattice beams from the perpendicular orientation. Considering the relation between the lattice spacings and the angles α_x and α_y between the lattice beams,

$$a_j = \frac{\lambda}{2} \frac{1}{\sin(\alpha_j/2)},$$

with $j = x, y$, we find a 6° deviation. Another modification from the ideal lattice potential given in Eq. (B1) comes from the uncoated glass cell, which reduces the power of the lattice beams (approximately 86 % transmission through each wall of the cell). By incorporating all these effects into a full band-structure calculation, we obtain an interaction strength U that differs by less than 3% from the value in the ideal model, and anisotropic tunnelings $J_x/h = 161(7)$ Hz and $J_y/h = 222(8)$ Hz. These parameters still correspond to the superfluid Hubbard regime, as discussed in the main text.

APPENDIX C: SPECTRUM OF RED COOLING COMPARED WITH FREE SPACE

To gain understanding of the cooling spectrum during site-resolved imaging, we compare the cooling frequencies with the free-space resonances at the magnetic field configuration ($\vec{B} \parallel \hat{\epsilon}_{813}$) that we use; see the main text. The free-space resonance is measured by shining resonant red light (689 nm) in the absence of any optical dipole trap potential and then determining the surviving atoms in absorption imaging.

The three resonances we measure correspond to the three m_J states of the 3P_1 excited state, displayed by the vertical lines in Fig. 6. The $m_J = \pm 1$ states are Zeeman-split from the $m_J = 0$ resonance by ±0.8 MHz and allow us to determine the magnitude of the magnetic field $B_z \approx 0.58$ G.

The spectrum of the cooling transition is inferred from the site-resolved fluorescence images, because atoms are cooled efficiently with attractive Sisyphus cooling only if the red cooling light is on or close to resonance. The measurement is performed along the same lines as the one reflected in Fig. 4. The three resonances at which we detect single atoms thanks to cooling are light-shifted due to the lattice and light-sheet potential. In this work we cool atoms

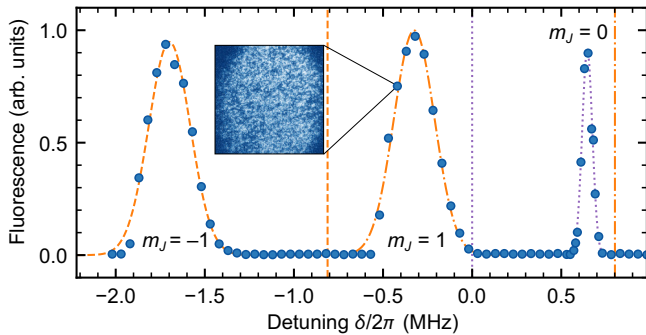


FIG. 6. Fluorescence spectrum of Sisyphus cooling. We detect the fluorescence of the atoms in the optical lattice (blue circles) for differing cooling frequencies detuned by δ from the free-space resonance of the $m_J = 0$ transition (vertical dotted line). The three peaks are fitted with three independent Gaussian functions, and correspond to the light-shifted m_J transitions of the 3P_1 excited state. The free-space resonance for the $|m_J| = 1$ transitions (vertical dashed and dot-dashed lines) are centered at around zero and are Zeeman-split by ± 0.8 MHz. Typically we detune the cooling light $\delta/2\pi \approx -0.4$ MHz from the free-space resonance in order to cool a large region; see the inset.

on the $m_J = 1$ transition, but the $m_J = -1$ transition works equivalently; see Fig. 6. The third resonance, corresponding to $m_J = 0$, is less effective in cooling. For this state, we have repulsive Sisyphus cooling due to its different polarizability compared with the $|m_J| = 1$ states.

We observe the maximum fluorescence signal of the $m_J = 1$ state $1.1(1)$ MHz shifted from its free-space resonance (dot-dashed vertical orange line in Fig. 6). While we typically perform cooling around this detuning, the light-shifted resonance at the center of the trap lies at the lower edge of the Gaussian fit, namely, at $\delta \approx -2\pi \times 0.5$ MHz. This corresponds to a 1.3-MHz detuning from its free-space resonance.

- [1] C. Gross and W. S. Bakr, Quantum gas microscopy for single atom and spin detection, *Nat. Phys.* **17**, 1316 (2021).
- [2] W. S. Bakr, A. Peng, M. E. Tai, R. Ma, J. Simon, J. I. Gillen, S. Fölling, L. Pollet, and M. Greiner, Probing the superfluid-to-Mott insulator transition at the single-atom level, *Science* **329**, 547 (2010).
- [3] J. F. Sherson, C. Weitenberg, M. Endres, M. Cheneau, I. Bloch, and S. Kuhr, Single-atom-resolved fluorescence imaging of an atomic Mott insulator, *Nature* **467**, 68 (2010).
- [4] E. Haller, J. Hudson, A. Kelly, D. A. Cotta, B. Peaudecerf, G. D. Bruce, and S. Kuhr, Single-atom imaging of fermions in a quantum-gas microscope, *Nat. Phys.* **11**, 738 (2015).
- [5] L. W. Cheuk, M. A. Nichols, M. Okan, T. Gersdorf, V. V. Ramasesh, W. S. Bakr, T. Lompe, and M. W. Zwierlein, Quantum-gas microscope for fermionic atoms, *Phys. Rev. Lett.* **114**, 193001 (2015).

- [6] M. F. Parsons, F. Huber, A. Mazurenko, C. S. Chiu, W. Setiawan, K. Wooley-Brown, S. Blatt, and M. Greiner, Site-resolved imaging of fermionic ${}^6\text{Li}$ in an optical lattice, *Phys. Rev. Lett.* **114**, 213002 (2015).
- [7] A. Omran, M. Boll, T. A. Hilker, K. Kleinlein, G. Salomon, I. Bloch, and C. Gross, Microscopic observation of Pauli blocking in degenerate Fermionic lattice gases, *Phys. Rev. Lett.* **115**, 263001 (2015).
- [8] J. Simon, W. S. Bakr, R. Ma, M. E. Tai, P. M. Preiss, and M. Greiner, Quantum simulation of antiferromagnetic spin chains in an optical lattice, *Nature* **472**, 307 (2011).
- [9] T. Fukuhara, A. Kantian, M. Endres, M. Cheneau, P. Schauß, S. Hild, D. Bellem, U. Schollwöck, T. Giamarchi, C. Gross, I. Bloch, and S. Kuhr, Quantum dynamics of a mobile spin impurity, *Nat. Phys.* **9**, 235 (2013).
- [10] A. Mazurenko, C. S. Chiu, G. Ji, M. F. Parsons, M. Kanász-Nagy, R. Schmidt, F. Grusdt, E. Demler, D. Greif, and M. Greiner, A cold-atom Fermi–Hubbard antiferromagnet, *Nature* **545**, 462 (2017).
- [11] D. Wei, A. Rubio-Abadal, B. Ye, F. Machado, J. Kemp, K. Srakaew, S. Hollerith, J. Rui, S. Gopalakrishnan, N. Y. Yao, I. Bloch, and J. Zeiher, Quantum gas microscopy of Kardar-Parisi-Zhang superdiffusion, *Science* **376**, 716 (2022).
- [12] P. T. Brown, D. Mitra, E. Guardado-Sánchez, R. Nourafkan, A. Reymbaut, C.-D. Hébert, S. Bergeron, A.-M. S. Tremblay, J. Kokalj, D. A. Huse, P. Schauß, and W. S. Bakr, Bad metallic transport in a cold atom Fermi-Hubbard system, *Science* **363**, 379 (2019).
- [13] M. A. Nichols, L. W. Cheuk, M. Okan, T. R. Hartke, E. Mendez, T. Senthil, E. Khatami, H. Zhang, and M. W. Zwierlein, Spin transport in a Mott insulator of ultracold fermions, *Science* **363**, 383 (2019).
- [14] E. Guardado-Sánchez, A. Morningstar, B. M. Spar, P. T. Brown, D. A. Huse, and W. S. Bakr, Subdiffusion and heat transport in a tilted two-dimensional Fermi-Hubbard system, *Phys. Rev. X* **10**, 011042 (2020).
- [15] A. M. Kaufman, M. E. Tai, A. Lukin, M. Rispoli, R. Schittko, P. M. Preiss, and M. Greiner, Quantum thermalization through entanglement in an isolated many-body system, *Science* **353**, 794 (2016).
- [16] J.-y. Choi, S. Hild, J. Zeiher, P. Schauß, A. Rubio-Abadal, T. Yefsah, V. Khemani, D. A. Huse, I. Bloch, and C. Gross, Exploring the many-body localization transition in two dimensions, *Science* **352**, 1547 (2016).
- [17] M. Rispoli, A. Lukin, R. Schittko, S. Kim, M. E. Tai, J. Léonard, and M. Greiner, Quantum critical behaviour at the many-body localization transition, *Nature* **573**, 385 (2019).
- [18] M. Miranda, R. Inoue, Y. Okuyama, A. Nakamoto, and M. Kozuma, Site-resolved imaging of ytterbium atoms in a two-dimensional optical lattice, *Phys. Rev. A* **91**, 063414 (2015).
- [19] R. Yamamoto, J. Kobayashi, T. Kuno, K. Kato, and Y. Takahashi, An ytterbium quantum gas microscope with narrow-line laser cooling, *New J. Phys.* **18**, 023016 (2016).
- [20] M. Miranda, R. Inoue, N. Tambo, and M. Kozuma, Site-resolved imaging of a bosonic Mott insulator using ytterbium atoms, *Phys. Rev. A* **96**, 043626 (2017).
- [21] L. Su, A. Douglas, M. Szurek, R. Groth, S. F. Ozturk, A. Krahn, A. H. Hébert, G. A. Phelps, S. Ebadi, S. Dickerson, F. Ferlaino, O. Marković, and M. Greiner, Dipolar quantum

- solids emerging in a Hubbard quantum simulator, *Nature* **622**, 724 (2023).
- [22] F. Schäfer, T. Fukuhara, S. Sugawa, Y. Takasu, and Y. Takahashi, Tools for quantum simulation with ultracold atoms in optical lattices, *Nat. Rev. Phys.* **2**, 411 (2020).
- [23] A. J. Daley, M. M. Boyd, J. Ye, and P. Zoller, Quantum computing with alkaline-earth-metal atoms, *Phys. Rev. Lett.* **101**, 170504 (2008).
- [24] M. A. Cazalilla and A. M. Rey, Ultracold Fermi gases with emergent $SU(N)$ symmetry, *Rep. Prog. Phys.* **77**, 124401 (2014).
- [25] L. F. Livi, G. Cappellini, M. Diem, L. Franchi, C. Clivati, M. Frittelli, F. Levi, D. Calonico, J. Catani, M. Inguscio, and L. Fallani, Synthetic dimensions and spin-orbit coupling with an optical clock transition, *Phys. Rev. Lett.* **117**, 220401 (2016).
- [26] S. Kolkowitz, S. L. Bromley, T. Bothwell, M. L. Wall, G. E. Marti, A. P. Koller, X. Zhang, A. M. Rey, and J. Ye, Spin-orbit-coupled fermions in an optical lattice clock, *Nature* **542**, 66 (2017).
- [27] T. Tomita, S. Nakajima, I. Danshita, Y. Takasu, and Y. Takahashi, Observation of the Mott insulator to superfluid crossover of a driven-dissipative Bose-Hubbard system, *Sci. Adv.* **3**, e1701513 (2017).
- [28] R. Bouganne, M. Bosch Aguilera, A. Ghermaoui, J. Beugnon, and F. Gerbier, Anomalous decay of coherence in a dissipative many-body system, *Nat. Phys.* **16**, 21 (2020).
- [29] S. Taie, R. Yamazaki, S. Sugawa, and Y. Takahashi, An $SU(6)$ Mott insulator of an atomic Fermi gas realized by large-spin Pomeranchuk cooling, *Nat. Phys.* **8**, 825 (2012).
- [30] C. Hofrichter, L. Riegger, F. Scazza, M. Höfer, D. R. Fernandes, I. Bloch, and S. Fölling, Direct probing of the Mott crossover in the $SU(N)$ Fermi-Hubbard model, *Phys. Rev. X* **6**, 021030 (2016).
- [31] S. L. Campbell, R. B. Hutson, G. E. Marti, A. Goban, N. Darkwah Oppong, R. L. McNally, L. Sonderhouse, J. M. Robinson, W. Zhang, B. J. Bloom, and J. Ye, A Fermi-degenerate three-dimensional optical lattice clock, *Science* **358**, 90 (2017).
- [32] S. Taie, E. Ibarra-García-Padilla, N. Nishizawa, Y. Takasu, Y. Kuno, H.-T. Wei, R. T. Scalettar, K. R. A. Hazzard, and Y. Takahashi, Observation of antiferromagnetic correlations in an ultracold $SU(N)$ Hubbard model, *Nat. Phys.* **18**, 1356 (2022).
- [33] S. Stellmer, M. K. Tey, B. Huang, R. Grimm, and F. Schreck, Bose-Einstein condensation of strontium, *Phys. Rev. Lett.* **103**, 200401 (2009).
- [34] Y. N. Martinez de Escobar, P. G. Mickelson, M. Yan, B. J. DeSalvo, S. B. Nagel, and T. C. Killian, Bose-Einstein condensation of ^{84}Sr , *Phys. Rev. Lett.* **103**, 200402 (2009).
- [35] B. J. DeSalvo, M. Yan, P. G. Mickelson, Y. N. Martinez de Escobar, and T. C. Killian, Degenerate Fermi gas of ^{87}Sr , *Phys. Rev. Lett.* **105**, 030402 (2010).
- [36] S. Stellmer, R. Grimm, and F. Schreck, Production of quantum-degenerate strontium gases, *Phys. Rev. A* **87**, 013611 (2013).
- [37] A. D. Ludlow, M. M. Boyd, J. Ye, E. Peik, and P. O. Schmidt, Optical atomic clocks, *Rev. Mod. Phys.* **87**, 637 (2015).
- [38] J. Ye, H. J. Kimble, and H. Katori, Quantum state engineering and precision metrology using state-insensitive light traps, *Science* **320**, 1734 (2008).
- [39] M. A. Norcia, A. W. Young, and A. M. Kaufman, Microscopic control and detection of ultracold strontium in optical-tweezer arrays, *Phys. Rev. X* **8**, 041054 (2018).
- [40] A. Cooper, J. P. Covey, I. S. Madjarov, S. G. Porosev, M. S. Safronova, and M. Endres, Alkaline-earth atoms in optical tweezers, *Phys. Rev. X* **8**, 041055 (2018).
- [41] N. Schine, A. W. Young, W. J. Eckner, M. J. Martin, and A. M. Kaufman, Long-lived Bell states in an array of optical clock qubits, *Nat. Phys.* **18**, 1067 (2022).
- [42] R. Tao, M. Ammenwerth, F. Gyer, I. Bloch, and J. Zeiher, High-fidelity detection of large-scale atom arrays in an optical lattice, *arXiv:2309.04717*.
- [43] A. W. Young, W. J. Eckner, N. Schine, A. M. Childs, and A. M. Kaufman, Tweezer-programmable 2D quantum walks in a Hubbard-regime lattice, *Science* **377**, 885 (2022).
- [44] A. W. Young, S. Geller, W. J. Eckner, N. Schine, S. Glancy, E. Knill, and A. M. Kaufman, An atomic boson sampler, *arXiv:2307.06936*.
- [45] F. Hu, I. Nosske, L. Couturier, C. Tan, C. Qiao, P. Chen, Y. H. Jiang, B. Zhu, and M. Weidmüller, Analyzing a single-laser repumping scheme for efficient loading of a strontium magneto-optical trap, *Phys. Rev. A* **99**, 033422 (2019).
- [46] T. P. Dinneen, K. R. Vogel, E. Arimondo, J. L. Hall, and A. Gallagher, Cold collisions of Sr^* –Sr in a magneto-optical trap, *Phys. Rev. A* **59**, 1216 (1999).
- [47] J. P. Covey, I. S. Madjarov, A. Cooper, and M. Endres, 2000-times repeated imaging of strontium atoms in clock-magic tweezer arrays, *Phys. Rev. Lett.* **122**, 173201 (2019).
- [48] J. Höschele, S. Buob, A. Rubio-Abadal, V. Makhalov, and L. Tarruell, Atom-number enhancement by shielding atoms from losses in strontium magneto-optical traps, *Phys. Rev. Appl.* **19**, 064011 (2023).
- [49] J. Sebby-Strabley, M. Anderlini, P. S. Jessen, and J. V. Porto, Lattice of double wells for manipulating pairs of cold atoms, *Phys. Rev. A* **73**, 033605 (2006).
- [50] P. T. Brown, D. Mitra, E. Guardado-Sánchez, P. Schauß, S. S. Kondov, E. Khatami, T. Paiva, N. Trivedi, D. A. Huse, and W. S. Bakr, Spin-imbalance in a 2D Fermi-Hubbard system, *Science* **357**, 1358 (2017).
- [51] J. Yang, L. Liu, J. Mongkolkiattichai, and P. Schauss, Site-resolved imaging of ultracold Fermions in a triangular-lattice quantum gas microscope, *PRX Quantum* **2**, 020344 (2021).
- [52] K. Kwon, K. Kim, J. Hur, S. J. Huh, and J. Y. Choi, Site-resolved imaging of a bosonic Mott insulator of ^7Li atoms, *Phys. Rev. A* **105**, 033323 (2022).
- [53] T. Ido and H. Katori, Recoil-free spectroscopy of neutral Sr atoms in the Lamb-Dicke regime, *Phys. Rev. Lett.* **91**, 053001 (2003).
- [54] R. Taïeb, R. Dum, J. I. Cirac, P. Marte, and P. Zoller, Cooling and localization of atoms in laser-induced potential wells, *Phys. Rev. A* **49**, 4876 (1994).
- [55] V. V. Ivanov and S. Gupta, Laser-driven Sisyphus cooling in an optical dipole trap, *Phys. Rev. A* **84**, 063417 (2011).
- [56] A. Urech, I. H. A. Knottnerus, R. J. C. Spreeuw, and F. Schreck, Narrow-line imaging of single strontium atoms in shallow optical tweezers, *Phys. Rev. Res.* **4**, 023245 (2022).

- [57] W. H. Richardson, Bayesian-based iterative method of image restoration, *J. Opt. Soc. Am.* **62**, 55 (1972).
- [58] L. B. Lucy, An iterative technique for the rectification of observed distributions, *Astron. J.* **79**, 745 (1974).
- [59] I. S. Madjarov, Ph.D. thesis, California Institute of Technology, 2021.
- [60] B. Capogrosso-Sansone, S. G. Söyler, N. Prokof'ev, and B. Svistunov, Monte Carlo study of the two-dimensional Bose-Hubbard model, *Phys. Rev. A* **77**, 015602 (2008).
- [61] M. Greiner, O. Mandel, T. Esslinger, T. W. Hänsch, and I. Bloch, Quantum phase transition from a superfluid to a Mott insulator in a gas of ultracold atoms, *Nature* **415**, 39 (2002).
- [62] H. Ozawa, R. Yamamoto, and T. Fukuhara, Observation of chiral-mode domains in a frustrated XY model on optical triangular lattices, *Phys. Rev. Res.* **5**, L042026 (2023).
- [63] P. A. Murthy, D. Kedar, T. Lompe, M. Neidig, M. G. Ries, A. N. Wenz, G. Zürn, and S. Jochim, Matter-wave Fourier optics with a strongly interacting two-dimensional Fermi gas, *Phys. Rev. A* **90**, 043611 (2014).
- [64] L. Franchi, L. F. Livi, G. Cappellini, G. Binella, M. Inguscio, J. Catani, and L. Fallani, State-dependent interactions in ultracold ^{174}Yb probed by optical clock spectroscopy, *New J. Phys.* **19**, 103037 (2017).
- [65] R. Bouganne, M. B. Aguilera, A. Dareau, E. Soave, J. Beugnon, and F. Gerbier, Clock spectroscopy of interacting bosons in deep optical lattices, *New J. Phys.* **19**, 113006 (2017).
- [66] G. E. Marti, R. B. Hutson, A. Goban, S. L. Campbell, N. Poli, and J. Ye, Imaging optical frequencies with 100 μHz precision and 1.1 μm resolution, *Phys. Rev. Lett.* **120**, 103201 (2018).
- [67] A. J. Park, J. Trautmann, N. Šantić, V. Klüsener, A. Heinz, I. Bloch, and S. Blatt, Cavity-enhanced optical lattices for scaling neutral atom quantum technologies to higher qubit numbers, *PRX Quantum* **3**, 030314 (2022).
- [68] J. Rui, D. Wei, A. Rubio-Abadal, S. Hollerith, J. Zeiher, D. M. Stamper-Kurn, C. Gross, and I. Bloch, A subradiant optical mirror formed by a single structured atomic layer, *Nature* **583**, 369 (2020).
- [69] R. B. Hutson, W. R. Milner, L. Yan, J. Ye, and C. Sanner, Observation of mHz-level cooperative Lamb shifts in an optical atomic clock, *Science* **383**, 384 (2024).
- [70] B. Olmos, D. Yu, Y. Singh, F. Schreck, K. Bongs, and I. Lesanovsky, Long-range interacting many-body systems with alkaline-earth-metal atoms, *Phys. Rev. Lett.* **110**, 143602 (2013).
- [71] T.-W. Zhou, G. Cappellini, D. Tusi, L. Franchi, J. Paravicini, C. Repellin, S. Greschner, M. Inguscio, T. Giarmachi, M. Filippone, J. Catani, and L. Fallani, Observation of universal Hall response in strongly interacting fermions, *Science* **381**, 427 (2023).
- [72] M. Hermele, V. Gurarie, and A. M. Rey, Mott insulators of ultracold fermionic alkaline earth atoms: Underconstrained magnetism and chiral spin liquid, *Phys. Rev. Lett.* **103**, 135301 (2009).
- [73] P. Corboz, A. M. Läuchli, K. Penc, M. Troyer, and F. Mila, Simultaneous dimerization and SU(4) symmetry breaking of 4-color fermions on the square lattice, *Phys. Rev. Lett.* **107**, 215301 (2011).
- [74] H. Katori, T. Ido, Y. Isoya, and M. Kuwata-Gonokami, Magneto-optical trapping and cooling of strontium atoms down to the photon recoil temperature, *Phys. Rev. Lett.* **82**, 1116 (1999).
- [75] M. A. Norcia, J. R. K. Cline, J. P. Bartolotta, M. J. Holland, and J. K. Thompson, Narrow-line laser cooling by adiabatic transfer, *New J. Phys.* **20**, 023021 (2018).
- [76] S. Snigirev, A. J. Park, A. Heinz, I. Bloch, and S. Blatt, Fast and dense magneto-optical traps for strontium, *Phys. Rev. A* **99**, 063421 (2019).
- [77] L. Tarruell, D. Greif, T. Uehlinger, G. Jotzu, and T. Esslinger, Creating, moving and merging Dirac points with a Fermi gas in a tunable honeycomb lattice, *Nature* **483**, 302 (2012).
- [78] D. Wei, D. Adler, K. Srakaew, S. Agrawal, P. Weckesser, I. Bloch, and J. Zeiher, Observation of brane parity order in programmable optical lattices, *Phys. Rev. X* **13**, 021042 (2023).